analytical chemistry

pubs.acs.org/ac Article

Hyperpolarized ^{129}Xe Atoms Sense the Presence of Drug Molecules in Nanohosts Revealed by Magnetic Resonance Imaging

Xu Zhang,[⊥] Yuqi Yang,[⊥] Yaping Yuan, Sen Yue, Xiuchao Zhao, Quer Yue, Qingbin Zeng, Qianni Guo, and Xin Zhou*

Cite This: https://doi.org/10.1021/acs.analchem.3c05573 Read Online

ACCESS | Metrics & More | Article Recommendations | Supporting Information

ABSTRACT: Assessing the effectiveness of nanomedicines involves evaluating the drug content at the target site. Currently, most research focuses on monitoring the signal responses from loaded drugs, neglecting the changes caused by the nanohosts. Here, we propose a strategy to quantitatively evaluate the content of loaded drugs by detecting the signal variations resulting from the alterations in the microenvironment of the nanohosts. Specifically, hyperpolarized (HP) ^{129}Xe atoms are employed as probes to sense the nanohosts' environment and generate a specific magnetic resonance (MR) signal that indicates their accessibility. The introduction of drugs reduces the available space in the nanohosts, leading to a crowded microenvironment that hinders the access of the ^{129}Xe atoms. By employing ^{129}Xe atoms as a signal source to detect the alterations in the microenvironment, we constructed a three-dimensional (3D) map that indicated the concentration of the nanohosts and established a linear relationship to quantitatively measure the drug content within the nanohosts based on the corresponding MR signals. Using the developed strategy, we successfully quantified the uptake of the nanohosts and drugs in living cells through HP ^{129}Xe MR imaging. Overall, the proposed HP ^{129}Xe atom-sensing approach can be used to monitor alterations in the microenvironment of nanohosts induced by loaded drugs and provides a new perspective for the quantitative evaluation of drug presence in various nanomedicines.

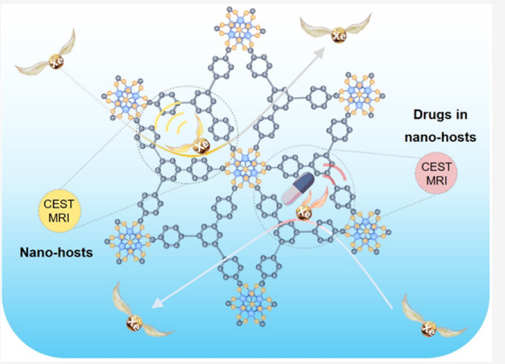

INTRODUCTION

Achieving the selective delivery of contrast agents and drug molecules to targeted areas is one of the toughest challenges for tumor imaging and treatment.[1−3] Typically, most of the drug molecules lack specific affinity toward a pathological site, leading to their widespread distribution throughout the body; this results in low tumor accumulation, swift blood clearance, substantial drug waste, and the onset of severe side effects.[4,5] Fortunately, nanotechnology provides promising solutions to address these obstacles by fabricating nanomedicines. In a typical nanomedicine, drug molecules are loaded into/onto nanocarriers, which can benefit from the active targeting of the functionalized groups,[6] the enhanced permeability and retention effect (EPR),[7] and the long blood circulation period of nanoparticles,[8] ultimately improving tumor imaging[9] and treatment efficacy.[10] However, most nanomedicines tend to accumulate and be cleared by normal organs such as the liver, kidney, and spleen before reaching the target lesion areas.[11] Furthermore, the issue of drug leakage during transportation further complicates the challenge of diminishing the overall drug content at the target site and causing adverse effects in healthy areas.[12] Therefore, evaluating the drug amount and loading efficiency of a nanomedicine upon arrival at the target field could be useful for assessing the effectiveness of nanomedicines.

Distance-responsible methods have been successfully developed to enable *in situ* detection of drug contents in nanocarriers.[13,14] An illustrative example involves using fluorescent drugs as electron donors, wherein the photon energy is transferred to the nanocarrier acceptors when the distance between the drug molecules and nanocarriers is less than 10 nm. This process effectively quenches the fluorescence of the drugs themselves.[15] Upon reaching the target site and being released from the nanocarriers, the fluorescence resonance energy transfer (FRET) effect disappears, resulting in the recovery of fluorescence.[16,17] The signal can also be controlled through aggregation-induced emission (AIE)[18] and aggregation-caused quenching (ACQ),[19] where the freedom of organic molecules is closely tied to their distance. This results in activated or quenched fluorescence as the drugs accumulate and self-assemble into nanoparticles in specific areas.[20] Due to the *in vivo* signal penetration limitations, MR-based techniques are considered more powerful for deep tissue and organ

Received: December 7, 2023
Revised: May 6, 2024
Accepted: May 22, 2024

Scheme 1. Hyperpolarized (HP) ^{129}Xe Spins Serve as a Probe to Sense the Microenvironment Changes in Nanohosts Induced by the Guest Drug Molecules[a]

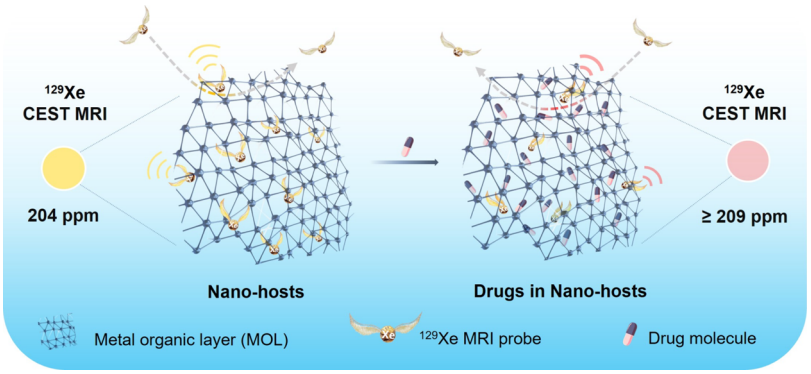

[a]HP ^{129}Xe atoms are able to move swiftly like the "Golden Snitches" in the Harry Potter movies when they freely traverse the environment. When interacting with reticulate MOL particles, they are able to smoothly pass through the artificially edited pores, sense the unique microenvironment of the nanohosts, and generate a specific magnetic resonance (MR) signal to indicate their presence. The introduction of drug molecules leads to a crowded microenvironment of the nanohosts, which slows the passage of ^{129}Xe atoms through the remaining free spaces and results in shifted MR signals. Thus, the HP ^{129}Xe atoms are capable of probing the alternations in the MOL nanohosts' microenvironment induced by the guest drug molecules through MR imaging.

detection.[21−23] Moreover, the MR signals can also be modulated by controlling the distance between the molecules and metals.[24] For instance, maintaining a close distance between the signal molecules and the paramagnetic Fe^{3+} and Gd^{3+} ions led to a reduction in the spin−lattice relaxation time (T_1) and an improved signal-to-noise ratio, facilitating rapid and effective ^{19}F MRI of fluorinated nanoemulsions.[25] In another design, gold nanoparticles served as an effective "shielding cover" for nuclear magnetic resonance spectroscopy (NMR) signals. Upon matching with the target ssDNA and being liberated from the nanoparticle surface, the NMR signal of ^{19}F-DNA was recovered.[26]

To date, much research on drug content in nanomedicines has focused primarily on monitoring signal responses originating from loaded molecules.[27] Minimal attention has been given to signal changes induced by nanocarriers because the departure of some drug molecules has a minimal impact on relatively large nanocarriers, causing challenges to detect the altered signal in nanoparticles. Additionally, the changes in the nanoparticle signals, such as fluorescent quantum dots,[28,29] photoacoustic microbubbles,[30] and magnetic Fe_3O_4 nanoparticles,[31] are often associated with structural collapse.[32] Consequently, a direct relationship between the signal response from nanocarriers and the content of loaded drugs is difficult to establish.

Herein, we propose the use of hyperpolarized xenon-129 (^{129}Xe) atoms as a signal source for probing the drug content in nanohosts through the detection of hyperpolarized magnetic resonance imaging (MRI) signals from nanocarriers. Compared to conventional MRI, hyperpolarized ^{129}Xe MRI provides enhanced sensitivity, reaching a signal gain up to 100,000 times.[33] Conventional MRI relies on signals from the spin −1/2 protons in a thermally polarized state, with only ∼1 out of every 100,000 nuclear spins (body temperature at 3 T) contributing to the detectable signal. Hyperpolarization amplifies the available magnetization by employing alkali metal as an intermediary to transfer angular momentum from photons to ^{129}Xe nuclei, disrupting the thermal equilibrium state,[34−36] rebalancing nuclear spins, and enabling the detection of at least 1 in 10 ^{129}Xe atoms (corresponding to a polarization value of 10% in this study).

Due to its significantly improved sensitivity, hyperpolarized (HP) ^{129}Xe MRI is referred to as ultrasensitive MRI.[37,38] HP ^{129}Xe MRI has proven to be an effective technique for enhancing anatomical contrast, especially in imaging void spaces such as the lungs.[39−41] Additionally, this technique has demonstrated significant success in molecular sensing applications,[42−44] achieving a detection limit in the sub-nanomolar range.[45−47] The remarkable sensitivity of ^{129}Xe atoms to their surrounding environment is particularly noteworthy,[48] with a chemical shift dispersion exceeding 5000 ppm, far surpassing that of ^{1}H NMR (∼10 ppm). Therefore, the HP ^{129}Xe MR techniques are able to distinguish the various microenvironments caused by the differences in porous materials.[49,50] Results from our study show that the exchange rate and charge effectively sensed by ^{129}Xe atoms could be modulated by regulating the skeleton structure of the metal−organic frameworks (MOFs), resulting in a specific ^{129}Xe MR signal in each tailored MOF.[51] Notably, the introduction of small molecules into the nanopores may alter the microenvironment due to the reduction in the pore size and the increase in crowding, which is anticipated to be distinguished by HP ^{129}Xe atoms.

In this study, we employed metal−organic layers (MOLs) as nanocarriers and demonstrated that the introduction of drug molecules hampered the accessibility of HP ^{129}Xe atoms to the nanohosts, resulting in a gradual shift and reduction in MR signal responses generated by guest ^{129}Xe (Scheme 1). The ^{129}Xe atoms, which move freely and rapidly, similar to the "Golden Snitches" in the Harry Potter movies, generate a signal at 193 ppm to confirm their presence in water. When the carefully designed MOLs are encountered, a specific signal at 204 ppm is induced. Using this distinct signal, we delineated a three-dimensional (3D) map to quantify the concentration of MOL through the corresponding ^{129}Xe MRI contrast. The introduction of drug molecules alters the microenvironments of the MOL nanohosts, which significantly affects the passage of ^{129}Xe atoms through the remaining free spaces. We demonstrated that the exchange rate between the surrounding free ^{129}Xe atoms and guest ^{129}Xe atoms in the nanohosts linearly decreased with increasing drug loading. More

https://doi.org/10.1021/acs.analchem.3c05573
Anal. Chem. XXXX, XXX, XXX−XXX

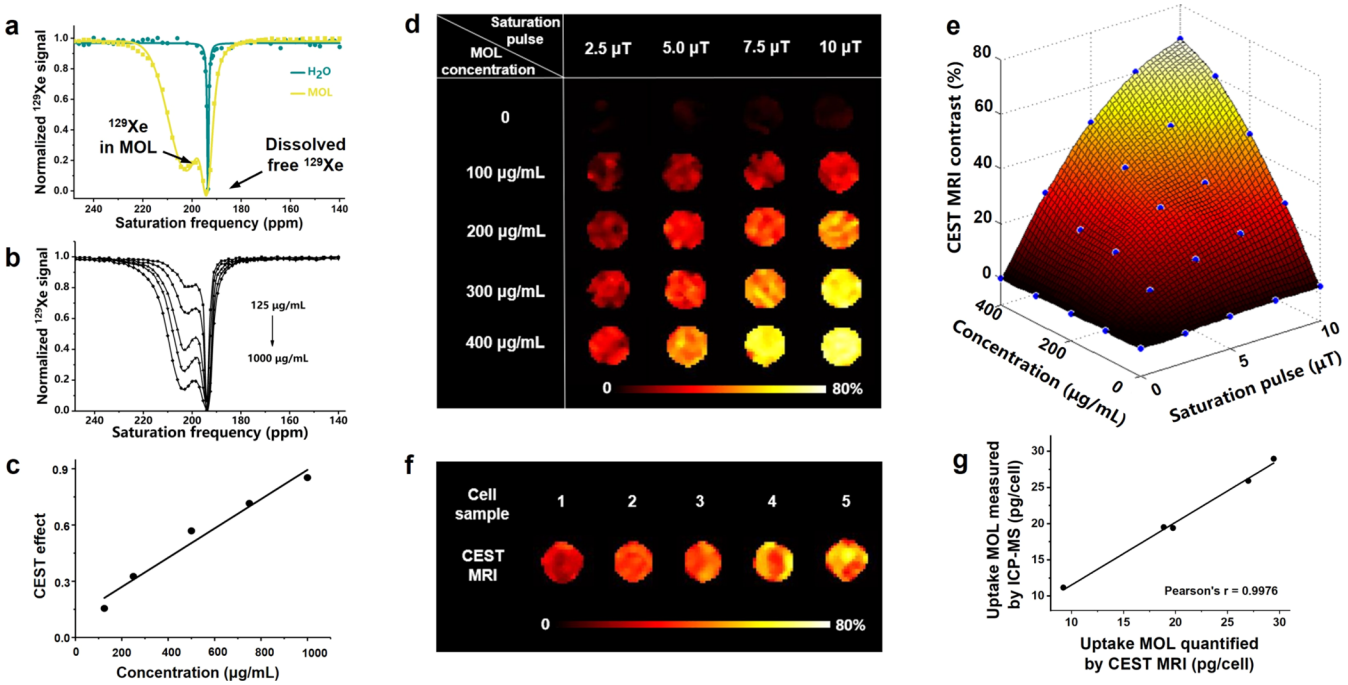

Figure 1. Quantitative analysis of the MOL concentration was carried out using HP ^{129}Xe CEST MRI. (a) HP ^{129}Xe CEST spectra of an aqueous solution (green) and an MOL dispersed aqueous solution (yellow). The specific signal at 204 ppm demonstrates the presence of ^{129}Xe atoms in the MOL nanohosts. (b) HP ^{129}Xe CEST spectra of MOL at concentrations of 125, 250, 500, 750, and 1000 μg/mL under a saturation pulse of 5 μT. (c) Linear relationship of the concentration of MOL to the CEST effect. (d) ^{129}Xe CEST MR images of the MOL nanohosts with various concentrations under a series of saturation pulses. (e) Establishment of a 3D map to describe the relationships between the ^{129}Xe CEST MRI contrast, MOL concentration, and saturation pulse. (f) ^{129}Xe CEST MRI of the cell samples under a saturation pulse of 10 μT. The cells were treated with different concentrations of the MOL medium. (g) Consistency analysis of the uptake MOL between the quantified values obtained by the ^{129}Xe CEST MRI-based 3D map and the measured values by ICP-MS.

importantly, the resulting signal changes were utilized to establish a linear correlation that enabled the calculation of the drug contents in the MOL nanohosts through the ^{129}Xe MRI contrast. The developed strategy was applied to quantify the content of the MOL nanohosts and drugs in living cells, yielding results that closely matched those obtained from inductively coupled plasma mass spectrometry (ICP-MS) and ultraviolet−visible (UV−vis) analysis, highlighting its potential applications in biological systems. Overall, we present a new approach for monitoring the presence of drugs in nanohosts by detecting MRI signals from competitive ^{129}Xe guests, providing a new perspective for evaluating the efficiency of nanomedicines from the viewpoint nanocarriers.

EXPERIMENTAL METHODS

Hyperpolarized ^{129}Xe NMR. Hyperpolarized ^{129}Xe gas was produced by a home-built ^{129}Xe hyperpolarizer (polarization 10%). A gas mixture of 10% N_2, 88% He, and 2% Xe (naturally abundant ^{129}Xe) was flowed through the hyperpolarizer; the resulting gas was guided to the 9.4 T Bruker AV400 widebore spectrometer and bubbled into the MOF dispersed solution at a flow rate of 0.1 L/min. The sample tube was maintained at a pressure of 53 PSI and a temperature of 298 K with the VT unit. During the HP ^{129}Xe CEST NMR experiments, the gas mixture was bubbled directly into the sample tube for 20 s. After a 3 s delay to allow the bubbles to collapse, continuous wave pulses (CW) were applied to selectively saturate the Xe@MOL peak (10 s with a 1−5 μT field). This was followed by the acquisition of a spectrum. Each spectrum was acquired in a single scan. NMR spectra for CEST were processed using a 6 Hz line broadening filter. Saturation frequencies are referenced to ^{129}Xe gas (0 ppm). Saturation contrast represents the normalized difference between the on-resonance and off-resonance signals. CEST effect = (Off-Resonance − On-Resonance)/Off-Resonance.

Hyperpolarized ^{129}Xe MRI. Production and ventilation processes of hyperpolarized ^{129}Xe are consistent with hyperpolarized ^{129}Xe NMR. ^{129}Xe MRI was generated with a RARE sequence with eight-echo trains and a 3 ms effective echo time. Including bubbling, wait, and saturation times, the overall repetition time (TR) was 28 s. 10 s CW saturation pulses with a field strength of 2.5 to 10 μT field were employed. All images were axial without slice selection, and the *k*-space matrix comprised 32 points in the readout dimension and 32 phase-encoding points. The field of view was 30 mm by 30 mm. The MR images were processed using in-house written Matlab scripts (R2014a, MathWorks, Natick, MA). The 32 × 32 image matrix was interpolated into a 64 × 64 matrix and segmented using 0.2 times the maximum value of the off-resonance image as the threshold. The CEST effect of each pixel was then calculated using the formula CEST effect = (Off-Resonance − On-Resonance)/Off-Resonance, pixel by pixel.

Cell Experiment. A549 cells were incubated with solutions of ICG, MOL, and ICG/MOL for 3 h, respectively. After removing the medium, the cells were carefully washed with sterile PBS for 3 times. Then, cells were carefully separated from the culture flask using a cell scraper. The obtained cells were dispersed in fresh F12K culture medium (containing 10% FBS, 1% penicillin−streptomycin) using a pipette, ensuring a smooth and repeated process to avoid generating gas bubbles. The cell dispersion solution was centrifuged at 300*g* for 3 min.

https://doi.org/10.1021/acs.analchem.3c05573
Anal. Chem. XXXX, XXX, XXX−XXX

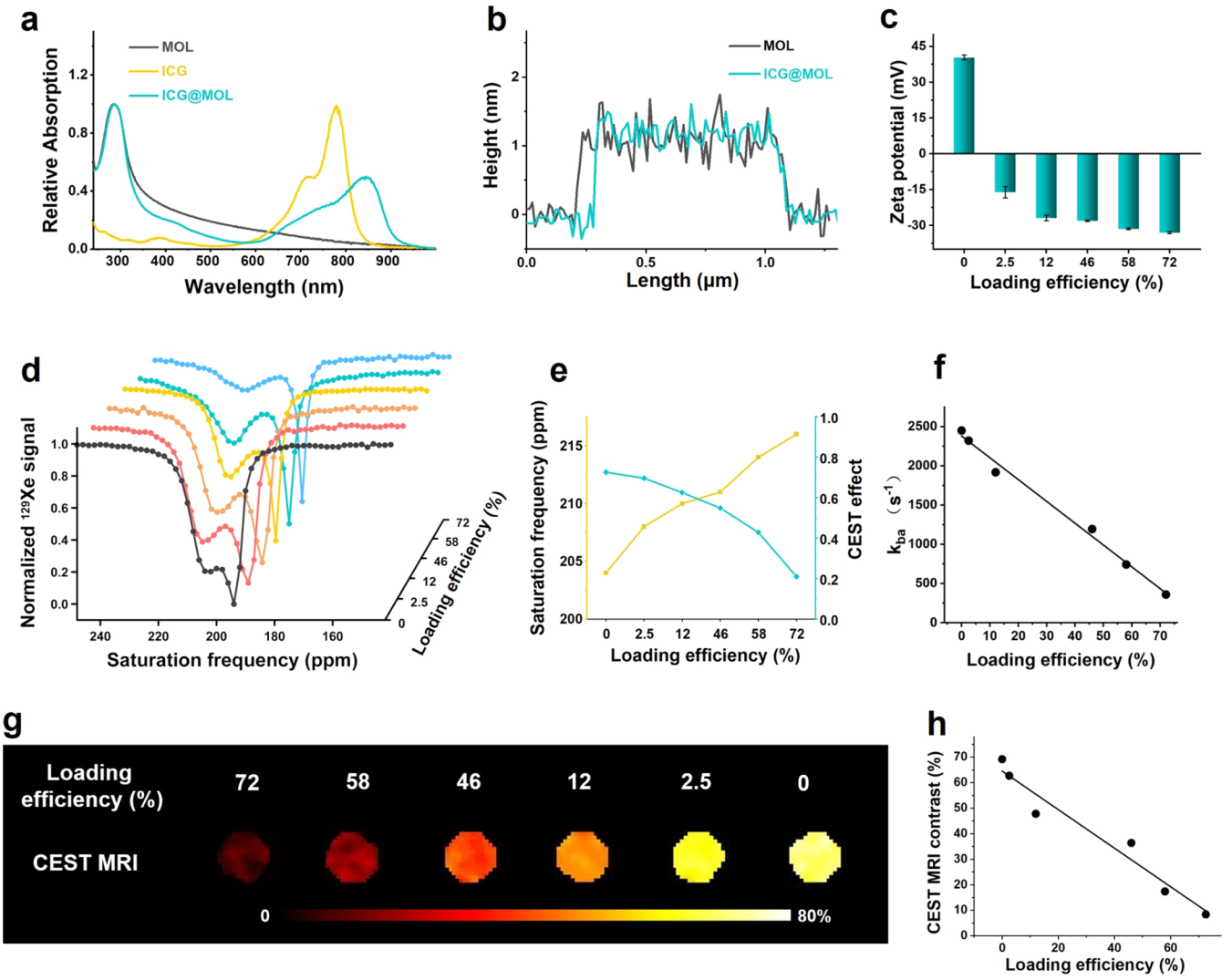

Figure 2. HP ^{129}Xe CEST MRI showing the environment changes of the MOL nanohosts induced by the introduction of drug molecules. (a) UV−vis spectra of MOL, ICG, and ICG-loaded MOL (ICG@MOL). (b) Thickness of MOL and ICG@MOL. (c) ζ-Potentials of ICG@MOL with various loading efficiencies. (d) CEST spectra of ICG@MOL with various loading efficiencies. (e) Continuous change of the saturation frequency and the CEST effect of the nanohosts with increasing drug loading efficiency. (f) Exchange rate (k_{ba}) between the incorporated ^{129}Xe atoms in ICG@MOL and the free ^{129}Xe atoms in the surrounding environment; the exchange rate is linear with respect to the loading efficiency. (g) Increase in the ^{129}Xe CEST MRI contrast with respect to the decreasing loading efficiency. (h) Linear relationship of the loading efficiency with respect to the CEST MRI contrast of the MOL nanohost.

After removing the supernatant, the cells were dispersed in PBS at a concentration of 1−2 × 10^7 cells/mL. Finally, 2 mL of the cell dispersion was transferred to an NMR tube for magnetic resonance analysis. After CEST MRI testing, the cells were collected and evaluated with ICP-MS for further quantitative analysis of MOL content.

RESULTS

Visitation of the ^{129}Xe Atoms to MOL Nanohosts and Generation of a Unique MR Signal. To investigate the exchange process of ^{129}Xe atoms between the surrounding environment and the nanohosts, we employed an MR sequence called chemical exchange saturation transfer (CEST); CEST amplified the target signal by measuring the decrease in the intensity of the free ^{129}Xe signal after selective saturation of ^{129}Xe within the host. As shown in Figure 1a, the free ^{129}Xe in water exhibited an MR signal at 193 ppm, while a new signal at 204 ppm appeared upon dispersion of MOL. This result confirmed our hypothesis that the HP ^{129}Xe atoms could sense the unique microenvironment established by the MOL nanohosts and generate a specific MR signal to indicate their presence. The exchange rate was determined to be 2450 ± 694 s^{-1} (Figure S7a); thus, the ultrathin layers facilitated rapid contact and exchange between the free ^{129}Xe atoms in the surrounding environment and guest ^{129}Xe in the MOL. Moreover, investigations into the target MR signal (204 ppm) revealed an enhanced CEST effect with increasing MOL concentration (Figure 1b), along with a linear response (Figure 1c). By utilization of the HP ^{129}Xe sensing approach, a detection limit of 10 μg/mL of MOL was achieved (Figure S8). Furthermore, the CEST effect exhibited only a fluctuation within 3% after 5 repeated experiments or storage for 60 days (Figure S9). These findings highlight the excellent MR response of ^{129}Xe in sensing the unique microenvironment of the MOL nanohosts with high sensitivity and stability.

https://doi.org/10.1021/acs.analchem.3c05573
Anal. Chem. XXXX, XXX, XXX−XXX

Quantification of the MOL Concentration Using the ^{129}Xe CEST MRI-Based 3D Map. The saturation pulse is another key factor that determines the CEST effect of Xe "host cages." As shown in Figure 1d, the ^{129}Xe CEST MR images produced from the MOL nanohosts as a function of the saturation pulse were carefully examined. The results showed a linear relationship between the corresponding contrast and the saturation pulse when the MOL concentration was determined (Figure S10a and Table S1). Additionally, the ^{129}Xe CEST MRI contrast showed linear relationships with the MOL concentration under a certain saturation power (between 2.5 and 10 μT) (Figure S10b and Table S2). Based on these results, a 3D map (Figure 1e) was generated to describe the relationship between the concentration of the MOL hosts, the saturation pulse, and the resulting CEST MRI contrast, with the aim to quantitatively evaluate the content of the MOL using ^{129}Xe CEST MRI.

To validate the efficacy of the 3D map, we exposed lung cancer A549 cells to the medium containing varying concentrations of MOL and subsequently subjected the samples to ^{129}Xe CEST MRI under a saturation pulse of 10 μT (Figure 1f). Then, the uptake MOL content could be quantified (Table S3) by entering the measured CEST MRI contrast into the 3D map. Remarkably, the uptake MOL contents quantified by the 3D map agreed closely with the results obtained from ICP-MS, with a Pearson's r of 0.9976 (Figure 1g).

^{129}Xe Guests Enabling Quantitative Imaging of Drug Content in Nanohosts. MOF-based nanomaterials have been extensively utilized as carriers in biomedical research for enhancing the targeting capabilities and/or achieving multifunctionality.[52−54] The study aimed to investigate interactions between two-dimensional (2D) MOF and drug molecules by detecting changes in nanohosts' microenvironments using HP ^{129}Xe atoms as probes, with ICG chosen as a representative model due to its widespread use in fluorescence-guided surgery[55] and photothermal studies.[56]

Upon successful loading of ICG into MOL, significant red shifts in the typical adsorption peaks of the molecule were observed (Figure 2a). The average thickness of ICG@MOL increased by only 0.15 nm compared with that of MOL (Figure 2b), indicating minimal multilayer stacking. Thus, the loaded ICG molecules were embedded within the nanopores rather than simply being adsorbed onto the surface of the MOL. Additionally, the inversion of the ζ-potential (Figure 2c) from positive to negative indicated that the loading of ICG altered the surface charge properties of the MOL.

As anticipated, the introduction of ICG resulted in a reduction in surface area (Figure S13) and a modification of the nanopore microenvironment in the MOL, decreasing the access of the free ^{129}Xe atoms to the nanohosts and triggering a cascade of changes in the MR signals. The MR signal at 204 ppm, representing the ^{129}Xe atoms in the MOL nanopores, immediately shifted to 209 ppm with a low loading efficiency of 2.5% (Figure 2d and Table 1). The increased content of ICG continuously altered the microenvironment of the nanopores, which could be detected by the guest ^{129}Xe atoms as the MR signals constantly shifted downfield (Figure 2e). Additionally, the CEST effect decreased with increasing loading efficacy, indicating a reduced exchange of the ^{129}Xe atoms due to the diminished free space within the MOL nanopores.

Table 1. ^{129}Xe-Host Interaction Parameters Obtained from Quantitative CEST[a]

loading efficiency (%)	ω_b (ppm)	fwhm$_b$ (Hz)	R_2^b (s^{-1})	k_{ba} (s^{-1})
0	204	10.1	120	2450 ± 694
2.5	209	11.3	836	2321 ± 472
12	210	13.3	1387	1917 ± 459
46	211	14.6	2380	1194 ± 356
58	214	19.1	4659	743 ± 186
72	215	24.3	8550	359 ± 168

[a]The increased content of drug molecules continuously altered the microenvironment of the nanohosts, which could be sensed by the ultrasensitive ^{129}Xe atoms and manifested as shifting downfield saturation frequency (ω_b), broadening full width at half-maximum (fwhm$_b$) and increasing transverse relaxation rate (R_2^b). Moreover, the exchange rate (k_{ba}) of ^{129}Xe atoms between the surrounding environment and the nanohosts decreased with the increasing drug loading efficiency.

Subsequently, we investigated the exchange dynamics between the free ^{129}Xe atoms in solution and the ^{129}Xe guests within MOL through a quantitative CEST analysis. As the loading efficiency increased, the MR signal of ^{129}Xe in the nanohosts exhibited a continuously broadening fwhm and an increasing transverse relaxation rate (R_2, Table 1). The exchange rate (k_{ba}) decreased from 2450 ± 694 to 359 ± 168 s^{-1} as the loading efficiency increased from 0 to 72%, showing a linear relationship (Figure 2f). The decrease in the exchange rate indicated that the occupation of drug molecules reduced the free space in the nanopores, hindering the passage of the ^{129}Xe atoms. Moreover, the corresponding MRI contrast increased with a decreasing loading efficiency (Figure 2g) and exhibited a linear relationship (Figure 2h).

HP ^{129}Xe Atoms Sensing the Presence of Drugs in Nanohosts within Living Cells. To evaluate the potential applicability of the designed approach for biological applications, we further investigated the signal response of the ^{129}Xe in nanohosts when drugs were introduced into the lung cancer A549 cells.

First, we confirmed that the ICG@MOL could be effectively taken up by A549 cells at the cellular level, in 3D cell spheres, and *in vivo* tumors (Figures S14−S22). Next, we conducted ^{129}Xe CEST MRI tests on the cells that were treated with ICG@MOL. The HP ^{129}Xe atoms exhibited a minimal response to the A549 lung cancer cells (Figure 3a), resulting in negligible MRI contrast. However, when these cells were treated with MOL, a strong signal with a CEST MRI contrast of 37.2% was observed (Figure 3b), indicating that the HP ^{129}Xe atoms were successfully hosted by the MOL within the cells. Interestingly, the stable microenvironment of the MOL nanohosts within living cells was further indicated by the specific MR signal retained at 204 ppm, which was comparable to that in an aqueous solution. Additionally, the MR signal evidently moved downfield when the cells were fed with ICG@MOL. Notably, the magnitude of MRI contrast depended on the drug loading efficiency, confirming the effectiveness of our designed approach as a quantitative method for monitoring the presence of drugs in the nanohosts within biological systems.

To further investigate the role of MOL, the A549 cells were first incubated with MOL for 2 h and then washed with PBS to remove any remaining MOL in the medium. Subsequently, the cells were treated with the medium containing ICG for an additional 2 h. The MRI results showed an evident contrast

https://doi.org/10.1021/acs.analchem.3c05573
Anal. Chem. XXXX, XXX, XXX−XXX

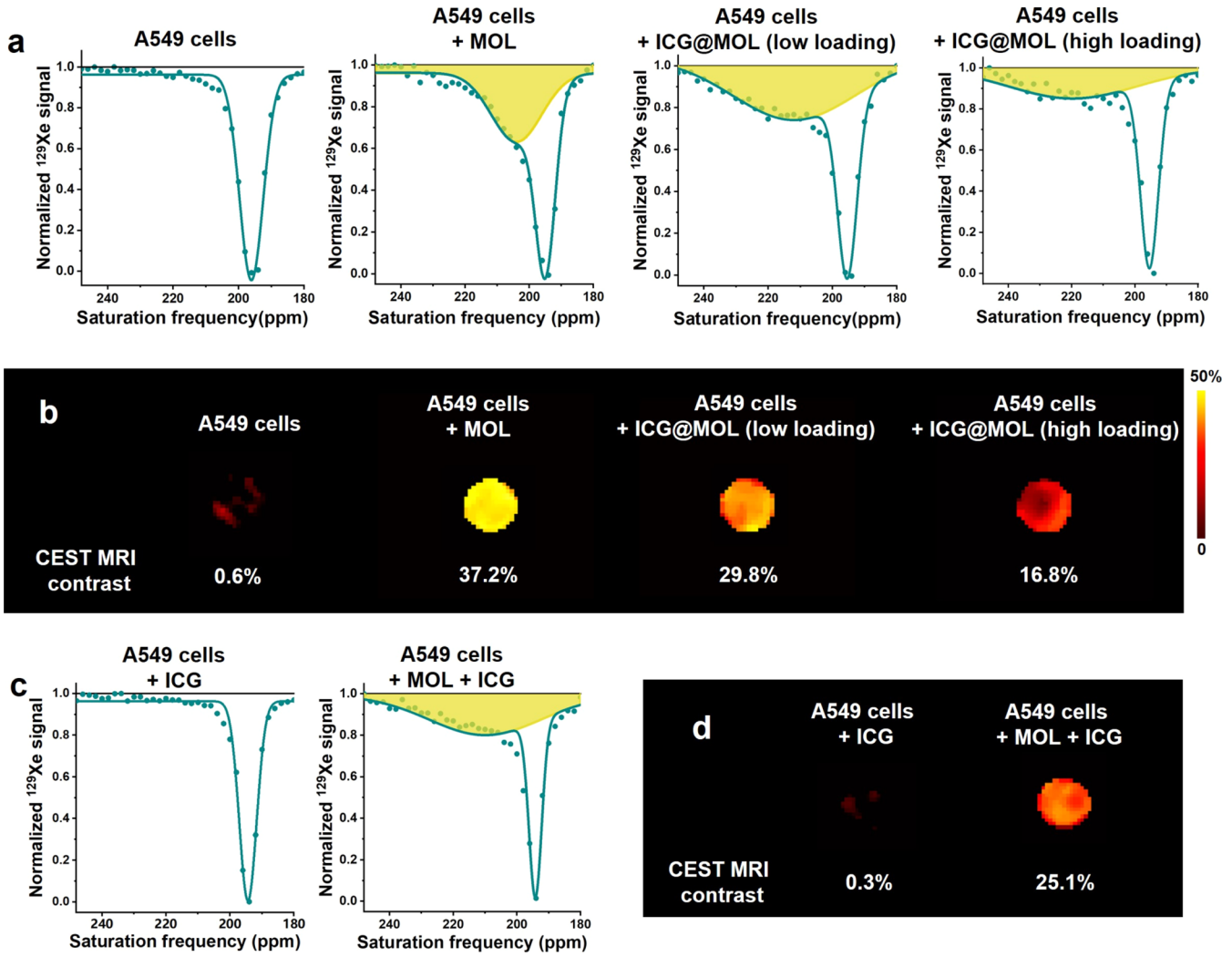

Figure 3. Detecting the presence of drug molecules in the nanohosts within live cells using HP ^{129}Xe CEST MRI. A549 cells were treated with MOL and ICG@MOL, respectively. Afterward, the cells were washed 3 times to eliminate any remaining nanomedicines, then suspended in F12K medium, and exposed to ^{129}Xe gas for CEST spectral analysis (a) and CEST MRI (b). Then, the capacity of MOL uptaken by cells to capture the drug molecules was evaluated using ^{129}Xe CEST MRI. The cells were treated with MOL for 2 h, followed by washing with PBS to remove the free MOL in medium. Subsequently, the cells were incubated with ICG for 2 h, the free ICG was removed, and then the cells were suspended in F12K medium and exposed to ^{129}Xe gas for CEST spectral analysis (c) and CEST MRI (d).

when probed by ^{129}Xe after ICG was introduced to the MOL-ingested A549 cells (Figure 3d). In contrast, in the absence of MOL, a detectable signal had difficulty being generated (Figure 3c). By analyzing the fitting results (Figure 2h), we quantified the amount of ICG hosted by MOL in the A549 cells with a loading efficiency of 16%. Moreover, further analysis using UV−vis and ICP-MS indicated that the mass ratio between ICG and MOL in A549 cells was 18%, which was slightly greater than the result obtained by ^{129}Xe CEST MRI.

DISCUSSION

The effectiveness of tumor imaging and treatment is heavily dependent on the drug content in the nanomedicines. Most current methods for evaluating drug content in nanocarriers involve detecting signals generated by the drugs. Here, we propose a novel approach that focuses on detecting changes in the microenvironment of nanohosts following the introduction of drugs. Our method utilizes HP ^{129}Xe atoms as probes and MR signal sources, which behave similarly to the "Golden Snitches" in the Harry Potter movies, moving freely. When these ^{129}Xe atoms encounter nanocarriers, they can penetrate the nanosized host spaces, generating distinct signals that distinguish them from those of free ^{129}Xe. The presence of drugs reduces the available space within the nanohosts, slowing the exchange of ^{129}Xe atoms and causing gradual shifts in MR signals.

In this study, the MOL nanohosts exhibited a specific MR signal at 204 ppm upon exposure to free ^{129}Xe (193 ppm). Based on the linear relationships among the ^{129}Xe CEST MRI contrast, MOL concentration, and saturation pulse, a 3D map was established to quantify the MOL concentration *via* the corresponding ^{129}Xe CEST MRI contrast. To explore its potential applications in biological systems, the validity of the 3D map was confirmed in living cells. The results demonstrated that the signal frequency generated by the cellular uptake of MOL remained consistent with that of water-dispersed MOL, regardless of the dispersion medium, as it was solely determined by the structure of the nanohost. Furthermore, the MOL uptake quantified using the ^{129}Xe

https://doi.org/10.1021/acs.analchem.3c05573
Anal. Chem. XXXX, XXX, XXX−XXX

CEST MRI-based 3D map closely correlated with the results obtained from ICP-MS analysis, exhibiting a Pearson's r value of 0.9976, thus affirming the reliability and effectiveness of the approach.

Next, the microenvironment changes in MOL nanohosts resulting from the introduction of ICG were investigated using the developed ^{129}Xe sensing approach. The increased loading efficiency continuously altered the microenvironment of the MOL nanohosts, leading to a consistent downfield saturation frequency shift and a decreased exchange rate of ^{129}Xe between the nanohosts and the surroundings. Notably, the resulting ^{129}Xe CEST MRI contrast showed a linear correlation with the loading efficiency, thereby serving as a standard for quantifying the ICG content in MOL nanohosts. Within living cells, the presence of ICG in MOL similarly caused a downfield saturation frequency shift and a reduction in the ^{129}Xe CEST MRI contrast, consistent with the observations in aqueous solutions. However, the ICG contents quantified by the developed ^{129}Xe sensing approach were slightly lower than those obtained by UV−vis and ICP-MS analyses. This difference may be attributed to a fraction of the uptake ICG not entering the MOL nanohosts, making it undetectable due to the lack of interaction with the specific designed microenvironments.

To explore the potential applications of the proposed approach in sensing other drugs, we conducted further investigations into the performance of ^{129}Xe CSET MRI on doxorubicin hydrochloride (DOX)- and protoporphyrin IX (PPIX)-loaded MOL. Similar to that of ICG, the specific MR signal of the MOL host shifted and decreased after the introduction of DOX (Figure S26) or PPIX (Figure S30). Additionally, the MRI contrast was linearly related to the loading efficiency (Figures S27 and S31). The three introduced drug molecules exhibited varying degrees of influence on the alteration of the nanohost microenvironment, as evident from the noticeable differences in the slopes of the fitting results. Based on these findings, we deduced that the CEST MRI contrast generated by the HP ^{129}Xe atoms in the MOL nanohosts was linearly correlated with the drug loading efficiency, which can be described by the following equation

$$M(x) = \alpha \cdot L(x) + M_0 \quad (1)$$

Here, $M(x)$ represents the determined ^{129}Xe CEST MRI contrast, α denotes the slope of the linear relationship, $L(x)$ represents the loading efficiency, and M_0 corresponds to the ^{129}Xe CEST MRI contrast for the bare MOL without any loaded drugs. In this study, we carefully measured the specific slopes for three model drugs, resulting in the following values: $\alpha_{ICG} = -0.7548$, $\alpha_{DOX} = -2.5849$, and $\alpha_{PPIX} = -4.1388$. By utilizing eq 1, the drug loading efficiency could be calculated by using the HP ^{129}Xe CEST MRI contrast.

In addition to a variety of loaded drug molecules, the proposed approach shows promise for characterizing other nanocarriers featuring regular nanopores suitable for hosting ^{129}Xe atoms. For instance, the specific structures of MOFs[57−59] and ordered porous nanomaterials[60,61] can effectively modulate the microenvironments required for ^{129}Xe atoms hosting. Consequently, distinct MR signals can be generated for each individual nanocarrier. These signals will undergo changes, and the changes can be detected upon the introduction of drug molecules, which reshape the microenvironments of the nanopores in these particles.

CONCLUSIONS AND PERSPECTIVES

In summary, the HP ^{129}Xe atom-sensing approach can be used to quantify the concentration of nanohosts by constructing a ^{129}Xe CEST MRI-based 3D map. Furthermore, it can successfully detect the loaded drug molecules as long as their presence alters the microenvironment of the nanohosts. This groundbreaking technique provides a promising new avenue for evaluating the presence and concentration of loaded drugs in biological systems and has tremendous potential for a wide array of nanomedicine applications. Numerous studies are expected to be conducted in the future, and they include but are not limited to the following. (1) Other well-dispersed 2D nanomaterials with different pore structures will be explored for HP ^{129}Xe MRI;[62,63] these materials may provide additional nanohosts for drug loading and generate a series of unique saturation frequencies to indicate the presence of drugs. (2) For 3D nanoparticles with good ^{129}Xe MR signals, such as ZIF-8 and IRMOFs,[33,51] surface modification may improve their dispersity and signal stability; thus, they may become more favorable nanohosts for drug loading and ^{129}Xe MRI detection. (3) By employing the next-generation near-unity HP ^{129}Xe hyperpolarizers together with >80% isotopic enrichment,[64,65] the NMR sensitivity of the experiment can be enhanced by 30-fold, which will further reduce the detection limit and provide additional benefits for future *in vivo* utilization with this new technology.

ASSOCIATED CONTENT

Supporting Information

The Supporting Information is available free of charge at https://pubs.acs.org/doi/10.1021/acs.analchem.3c05573.

Preparation and characterization of MOL nanohosts; procedures of ^{129}Xe CEST NMR and ^{129}Xe CEST MRI tests; drug loading methods and characterization; cell culture and uptake experiments; *in vivo* fluorescent imaging, photoacoustic imaging, and biosafety studies; and ^{129}Xe CEST tests and analysis of hydrochloride and protoporphyrin IX in MOL nanohosts (PDF)

AUTHOR INFORMATION

Corresponding Author

Xin Zhou − *Key Laboratory of Magnetic Resonance in Biological Systems, State Key Laboratory of Magnetic Resonance and Atomic and Molecular Physics, National Center for Magnetic Resonance in Wuhan, Wuhan Institute of Physics and Mathematics, Innovation Academy for Precision Measurement Science and Technology, Wuhan 430071, China; University of Chinese Academy of Sciences, Beijing 100049, China;* orcid.org/0000-0002-5580-7907; Email: xinzhou@wipm.ac.cn

Authors

Xu Zhang − *Key Laboratory of Magnetic Resonance in Biological Systems, State Key Laboratory of Magnetic Resonance and Atomic and Molecular Physics, National Center for Magnetic Resonance in Wuhan, Wuhan Institute of Physics and Mathematics, Innovation Academy for Precision Measurement Science and Technology, Wuhan 430071, China; University of Chinese Academy of Sciences, Beijing 100049, China*

Yuqi Yang − *Key Laboratory of Magnetic Resonance in Biological Systems, State Key Laboratory of Magnetic*

https://doi.org/10.1021/acs.analchem.3c05573
Anal. Chem. XXXX, XXX, XXX−XXX

Resonance and Atomic and Molecular Physics, National Center for Magnetic Resonance in Wuhan, Wuhan Institute of Physics and Mathematics, Innovation Academy for Precision Measurement Science and Technology, Wuhan 430071, China; University of Chinese Academy of Sciences, Beijing 100049, China

Yaping Yuan − *Key Laboratory of Magnetic Resonance in Biological Systems, State Key Laboratory of Magnetic Resonance and Atomic and Molecular Physics, National Center for Magnetic Resonance in Wuhan, Wuhan Institute of Physics and Mathematics, Innovation Academy for Precision Measurement Science and Technology, Wuhan 430071, China*

Sen Yue − *Key Laboratory of Magnetic Resonance in Biological Systems, State Key Laboratory of Magnetic Resonance and Atomic and Molecular Physics, National Center for Magnetic Resonance in Wuhan, Wuhan Institute of Physics and Mathematics, Innovation Academy for Precision Measurement Science and Technology, Wuhan 430071, China; University of Chinese Academy of Sciences, Beijing 100049, China*

Xiuchao Zhao − *Key Laboratory of Magnetic Resonance in Biological Systems, State Key Laboratory of Magnetic Resonance and Atomic and Molecular Physics, National Center for Magnetic Resonance in Wuhan, Wuhan Institute of Physics and Mathematics, Innovation Academy for Precision Measurement Science and Technology, Wuhan 430071, China*

Quer Yue − *Key Laboratory of Magnetic Resonance in Biological Systems, State Key Laboratory of Magnetic Resonance and Atomic and Molecular Physics, National Center for Magnetic Resonance in Wuhan, Wuhan Institute of Physics and Mathematics, Innovation Academy for Precision Measurement Science and Technology, Wuhan 430071, China*

Qingbin Zeng − *Key Laboratory of Magnetic Resonance in Biological Systems, State Key Laboratory of Magnetic Resonance and Atomic and Molecular Physics, National Center for Magnetic Resonance in Wuhan, Wuhan Institute of Physics and Mathematics, Innovation Academy for Precision Measurement Science and Technology, Wuhan 430071, China*

Qianni Guo − *Key Laboratory of Magnetic Resonance in Biological Systems, State Key Laboratory of Magnetic Resonance and Atomic and Molecular Physics, National Center for Magnetic Resonance in Wuhan, Wuhan Institute of Physics and Mathematics, Innovation Academy for Precision Measurement Science and Technology, Wuhan 430071, China*

Complete contact information is available at: https://pubs.acs.org/10.1021/acs.analchem.3c05573

Author Contributions

[⊥]Y. Y. and X. Z. contributed equally to this work. Y.Y. conceived and designed the project and prepared the manuscript. X.Z. collected the majority of the data. Y.Y. and X.Z. conducted data analyses. Y.Y. assisted with the analysis of NMR and MRI results. S.Y. and Q.Y. provided assistance with cell and animal experiments. X.Z. constructed the hyperpolarizer instrument utilized in this study. Q.G. and Q.Z. aided in proofing the manuscript. X.Z. supervised the project.

Notes

The authors declare no competing financial interest.

■ ACKNOWLEDGMENTS

This work was supported by the National Natural Science Foundation of China (82127802, 22274162, and 21921004), the National Key R&D Program of China (2018YFA0704000), the Key Research Program of Frontier Sciences, CAS (ZDBS-LY-JSC004), the Strategic Priority Research Program, CAS (XDB0540000), and the Hubei Provincial Key Technology Foundation of China (2021ACA013). Y.Y. acknowledges the support from the Youth Innovation Promotion Association, CAS (2022336); Q.G. acknowledges the support from the CAS Youth Interdisciplinary Team (JCTD-2022-13).

■ REFERENCES

(1) Mitchell, M. J.; Billingsley, M. M.; Haley, R. M.; Wechsler, M. E.; Peppas, N. A.; Langer, R. *Nat. Rev. Drug Discovery* **2021**, *20*, 101−124.
(2) Song, W.; Zheng, D.; Zeng, S.; Zeng, X.; Zhang, X. *ACS Nano* **2022**, *16*, 17402−17413.
(3) Wang, H.; Xu, S.; Fan, D.; Geng, X.; Zhi, G.; Wu, D.; Shen, H.; Yang, F.; Zhou, X.; Wang, X. *Bioact. Mater.* **2022**, *7*, 453−465.
(4) Wilhelm, S.; Tavares, A. J.; Dai, Q.; Ohta, S.; Audet, J.; Dvorak, H. F.; Chan, W. C. W. *Nat. Rev. Mater.* **2016**, *1*, No. 16014.
(5) Yue, Y.; Zhang, Z.; Wang, Z.; Ma, R.; Chen, M.; Ding, F.; Li, H.; Li, J.; Shi, L.; Liu, Y.; Guo, D. *Small Struct.* **2022**, *3*, No. 2200067.
(6) Wang, L.; Shi, Y.; Jiang, J.; Li, C.; Zhang, H.; Zhang, X.; Jiang, T.; Wang, L.; Wang, Y.; Feng, L. *Small* **2022**, *18*, No. e2203678.
(7) Zi, Y.; Yang, K.; He, J.; Wu, Z.; Liu, J.; Zhang, W. *Adv. Drug Delivery Rev.* **2022**, *188*, No. 114449.
(8) Wen, M.; Yu, N.; Wu, S.; Huang, M.; Qiu, P.; Ren, Q.; Zhu, M.; Chen, Z. *Bioact. Mater.* **2022**, *18*, 242−253.
(9) Li, T.; Tan, S.; Li, M.; Luo, J.; Zhang, Y.; Jiang, Z.; Deng, Y.; Han, L.; Ke, H.; Shen, J.; Tang, Y.; Liu, F.; Chen, H.; Yang, T. *Adv. Mater.* **2023**, *35*, No. e2209603.
(10) Yang, J.; Li, Y.; Sun, J.; Zou, H.; Sun, Y.; Luo, J.; Xie, Q.; A, R.; Wang, H.; Li, X.; Wang, K.; Yang, L.; Ma, T.; Wu, L.; Sun, X. *ACS Nano* **2022**, *16*, 12590−12605.
(11) Martin, J. D.; Cabral, H.; Stylianopoulos, T.; Jain, R. K. *Nat. Rev. Clin. Oncol.* **2020**, *17*, 251−266.
(12) Irvine, D. J.; Dane, E. L. *Nat. Rev. Immunol.* **2020**, *20*, 321−334.
(13) Song, N.; Zhang, Z.; Liu, P.; Yang, Y. W.; Wang, L.; Wang, D.; Tang, B. Z. *Adv. Mater.* **2020**, *32*, No. e2004208.
(14) Alhaidari, L. M.; Spain, S. G. *Polymers* **2023**, *15*, No. 1778.
(15) Klymchenko, A. S.; Liu, F.; Collot, M.; Anton, N. *Adv. Healthcare Mater.* **2021**, *10*, No. e2001289.
(16) Kaeokhamloed, N.; Legeay, S.; Roger, E. *J. Controlled Release* **2022**, *349*, 156−173.
(17) Kurniawan, D.; Mathew, J.; Rahardja, M. R.; Pham, H. P.; Wong, P. C.; Rao, N. V.; Ostrikov, K. K.; Chiang, W. H. *Small* **2023**, *19*, No. e2206813.
(18) Feng, Z.; Bai, S.; Qi, J.; Sun, C.; Zhang, Y.; Yu, X.; Ni, H.; Wu, D.; Fan, X.; Xue, D.; Liu, S.; Chen, M.; Gong, J.; Wei, P.; He, M.; Lam, J. W. Y.; Li, X.; Tang, B. Z.; Gao, L.; Qian, J. *Adv. Mater.* **2021**, *33*, No. e2008123.
(19) Qi, J.; Hu, X.; Dong, X.; Lu, Y.; Lu, H.; Zhao, W.; Wu, W. *Adv. Drug Delivery Rev.* **2019**, *143*, 206−225.
(20) Wu, H.; Zhang, L.; Yang, J.; Bo, R.; Du, H.; Lin, K.; Zhang, D.; Ramachandran, M.; Shen, Y.; Xu, Y.; Xue, X.; Ma, Z.; Lindstrom, A. R.; Carney, R.; Lin, T. Y.; Li, Y. *Adv. Funct. Mater.* **2020**, *30*, No. 1910348.
(21) Otazo, R.; Lambin, P.; Pignol, J. P.; Ladd, M. E.; Schlemmer, H. P.; Baumann, M.; Hricak, H. *Radiology* **2021**, *298*, 248−260.
(22) Wahsner, J.; Gale, E. M.; Rodríguez-Rodríguez, A.; Caravan, P. *Chem. Rev.* **2019**, *119*, 957−1057.

(23) Zhang, C.; Yan, K.; Fu, C.; Peng, H.; Hawker, C. J.; Whittaker, A. K. *Chem. Rev.* **2022**, *122*, 167−208.
(24) Chen, B.; Liu, L.; Yue, R.; Dong, Z.; Lu, C.; Zhang, C.; Guan, G.; Liu, H.; Zhang, Q.; Song, G. *Nano Today* **2023**, *51*, No. 101931.
(25) Kislukhin, A. A.; Xu, H.; Adams, S. R.; Narsinh, K. H.; Tsien, R. Y.; Ahrens, E. T. *Nat. Mater.* **2016**, *15*, 662−668.
(26) Kieger, A.; Wiester, M. J.; Procissi, D.; Parrish, T. B.; Mirkin, C. A.; Thaxton, C. S. *Small* **2011**, *7*, 1977−1981.
(27) Zheng, F.; Xiong, W.; Sun, S.; Zhang, P.; Zhu, J. *Nanophotonics* **2019**, *8*, 391−413.
(28) Wang, P.; Li, J.; Wei, M.; Yang, R.; Lou, K.; Dang, Y.; Sun, W.; Xue, F.; Liu, X. *Biomaterials* **2022**, *287*, No. 121636.
(29) Yang, Y.; Wang, B.; Zhang, X.; Li, H.; Yue, S.; Zhang, Y.; Yang, Y.; Liu, M.; Ye, C.; Huang, P.; Zhou, X. *Adv. Mater.* **2023**, *35*, No. e2211337.
(30) Fan, K.; Zeng, L.; Guo, J.; Xie, S.; Yu, Y.; Chen, J.; Cao, J.; Xiang, Q.; Zhang, S.; Luo, Y.; Deng, Q.; Zhou, Q.; Zhao, Y.; Hao, L.; Wang, Z.; Zhong, L. *Theranostics* **2021**, *11*, 2670−2690.
(31) Zhang, P.; Qiao, Y.; Zhu, L.; Qin, M.; Li, Q.; Liu, C.; Xu, Y.; Zhang, X.; Gan, Z.; Hou, Y. *ACS Nano* **2023**, *17*, 184−196.
(32) Song, S.; Wang, Q.; Xie, J.; Dai, J.; Ouyang, D.; Huang, G.; Guo, Y.; Chen, C.; Wu, M.; Huang, T.; Ruan, J.; Cheng, X.; Lin, X.; He, Y.; Rozhkova, E. A.; Chen, Z.; Yang, H. *Adv. Healthcare Mater.* **2023**, *12*, No. e2301437.
(33) Zeng, Q.; Bie, B.; Guo, Q.; Yuan, Y.; Han, Q.; Han, X.; Chen, M.; Zhang, X.; Yang, Y.; Liu, M.; Liu, P.; Deng, H.; Zhou, X. *Proc. Natl. Acad. Sci. U.S.A.* **2020**, *117*, 17558−17563.
(34) Zeng, X.; Wu, Z.; Call, T.; Miron, E.; Schreiber, D.; Happer, W. *Phys. Rev. A* **1985**, *31*, 260−278.
(35) Whiting, N.; Eschmann, N. A.; Goodson, B. M.; Barlow, M. J. *Phys. Rev. A* **2011**, *83*, No. 053428.
(36) Witte, C.; Kunth, M.; Döpfert, J.; Rossella, F.; Schröder, L. *J. Visualized Exp.* **2012**, *67*, No. e4268.
(37) Kunth, M.; Witte, C.; Hennig, A.; Schröder, L. *Chem. Sci.* **2015**, *6*, 6069−6075.
(38) Wang, Y.; Roose, B. W.; Palovcak, E. J.; Carnevale, V.; Dmochowski, I. J. *Angew. Chem., Int. Ed.* **2016**, *55*, 8984−8987.
(39) Khan, A. S.; Harvey, R. L.; Birchall, J. R.; Irwin, R. K.; Nikolaou, P.; Schrank, G.; Emami, K.; Dummer, A.; Barlow, M. J.; Goodson, B. M.; Chekmenev, E. Y. *Angew. Chem., Int. Ed.* **2021**, *60*, 22126−22147.
(40) Kooner, H. K.; McIntosh, M. J.; Matheson, A. M.; Abdelrazek, M.; Albert, M. S.; Dhaliwal, I.; Kirby, M.; Ouriadov, A.; Santyr, G. E.; Venegas, C.; Radadia, N.; Svenningsen, S.; Nicholson, J. M.; Parraga, G. *Radiology* **2023**, *307*, No. e222557.
(41) McIntosh, M. J.; Kooner, H. K.; Eddy, R. L.; Jeimy, S.; Licskai, C.; Mackenzie, C. A.; Svenningsen, S.; Nair, P.; Yamashita, C.; Parraga, G. *Chest* **2022**, *162*, 520−533.
(42) Spence, M. M.; Rubin, S. M.; Dimitrov, I. E.; Ruiz, E. J.; Wemmer, D. E.; Pines, A.; Yao, S. Q.; Tian, F.; Schultz, P. G. *Proc. Natl. Acad. Sci. U.S.A.* **2001**, *98*, 10654−10657.
(43) Witte, C.; Martos, V.; Rose, H. M.; Reinke, S.; Klippel, S.; Schröder, L.; Hackenberger, C. P. *Angew. Chem., Int. Ed.* **2015**, *54*, 2806−2810.
(44) Schnurr, M.; Sloniec-Myszk, J.; Döpfert, J.; Schröder, L.; Hennig, A. *Angew. Chem., Int. Ed.* **2015**, *54*, 13444−13447.
(45) Schröder, L.; Lowery, T. J.; Hilty, C.; Wemmer, D. E.; Pines, A. *Science* **2006**, *314*, 446−449.
(46) Shapiro, M. G.; Ramirez, R. M.; Sperling, L. J.; Sun, G.; Sun, J.; Pines, A.; Schaffer, D. V.; Bajaj, V. S. *Nat. Chem.* **2014**, *6*, 629−634.
(47) Roose, B. W.; Zemerov, S. D.; Dmochowski, I. J. *Chem. Sci.* **2017**, *8*, 7631−7636.
(48) Jayapaul, J.; Komulainen, S.; Zhivonitko, V. V.; Mares, J.; Giri, C.; Rissanen, K.; Lantto, P.; Telkki, V. V.; Schröder, L. *Nat. Commun.* **2022**, *13*, No. 1708.
(49) Wisser, D.; Hartmann, M. *Adv. Mater. Interfaces* **2021**, *8*, No. 2001266.
(50) Li, J.; Mailhiot, S.; Sreenivasan, H.; Kantola, A. M.; Telkki, V. V.; Kinnunen, P. *Cem. Concr. Res.* **2022**, *155*, No. 106779.
(51) Yang, Y.; Zhang, Y.; Wang, B.; Guo, Q.; Yuan, Y.; Jiang, W.; Shi, L.; Yang, M.; Chen, S.; Lou, X.; Zhou, X. *Chem. Sci.* **2021**, *12*, 4300−4308.
(52) Mao, D.; Hu, F.; Kenry; Ji, S.; Wu, W.; Ding, D.; Kong, D.; Liu, B. *Adv. Mater.* **2018**, *30*, No. 1870124.
(53) Sun, Y.; Zheng, L.; Yang, Y.; Qian, X.; Fu, T.; Li, X.; Yang, Z.; Yan, H.; Cui, C.; Tan, W. *Nano-Micro Lett.* **2020**, *12*, No. 103.
(54) Zhao, Q.; Gong, Z.; Li, Z.; Wang, J.; Zhang, J.; Zhao, Z.; Zhang, P.; Zheng, S.; Miron, R. J.; Yuan, Q.; Zhang, Y. *Adv. Mater.* **2021**, *33*, No. e2100616.
(55) Wakabayashi, T.; Cacciaguerra, A. B.; Abe, Y.; Bona, E. D.; Nicolini, D.; Mocchegiani, F.; Kabeshima, Y.; Vivarelli, M.; Wakabayashi, G.; Kitagawa, Y. *Ann. Surg.* **2022**, *275*, 1025−1034.
(56) Chen, Q.; Xu, L.; Liang, C.; Wang, C.; Peng, R.; Liu, Z. *Nat. Commun.* **2016**, *7*, No. 13193.
(57) Trepte, K.; Schaber, J.; Schwalbe, S.; Drache, F.; Senkovska, I.; Kaskel, S.; Kortus, J.; Brunner, E.; Seifert, G. *Phys. Chem. Chem. Phys.* **2017**, *19*, 10020−10027.
(58) Hoffmann, H. C.; Assfour, B.; Epperlein, F.; Klein, N.; Paasch, S.; Senkovska, I.; Kaskel, S.; Seifert, G.; Brunner, E. *J. Am. Chem. Soc.* **2011**, *133*, 8681−8690.
(59) Bunzen, H.; Jirak, D. *ACS Appl. Mater. Interfaces* **2022**, *14*, 50445−50462.
(60) Jabbour, R.; Ashling, C.; Robinson, T.; Khan, A. H.; Wisser, D.; Berruyer, P.; Ghosh, A. C.; Ranscht, A.; Keen, D. A.; Brunner, E.; Canivet, J.; Bennett, T. D.; Mellot-Draznieks, C.; Lesage, A.; Wisser, F. M. *Angew. Chem., Int. Ed.* **2023**, *62*, No. e202310878.
(61) Hollenbach, J.; Küster, C.; Uhlig, H.; Wagner, M.; Abel, B.; Gläser, R.; Einicke, W. D.; Enke, D.; Matysik, J. *J. Phys. Chem. C* **2017**, *121*, 15804−15814.
(62) Chakraborty, G.; Park, I. H.; Medishetty, R.; Vittal, J. J. *Chem. Rev.* **2021**, *121*, 3751−3891.
(63) Sakamoto, R.; Fukui, N.; Maeda, H.; Toyoda, R.; Takaishi, S.; Tanabe, T.; Komeda, J.; Amo-Ochoa, P.; Zamora, F.; Nishihara, H. *Coord. Chem. Rev.* **2022**, *472*, No. 214787.
(64) Nikolaou, P.; Coffey, A. M.; Walkup, L. L.; Gust, B. M.; Whiting, N.; Newton, H.; Barcus, S.; Muradyan, I.; Dabaghyan, M.; Moroz, G. D.; Rosen, M. S.; Patz, S.; Barlow, M. J.; Chekmenev, E. Y.; Goodson, B. M. *Proc. Natl. Acad. Sci. U.S.A.* **2013**, *110*, 14150−14155.
(65) Birchall, J. R.; Irwin, R. K.; Nikolaou, P.; Coffey, A. M.; Kidd, B. E.; Murphy, M.; Molway, M.; Bales, L. B.; Ranta, K.; Barlow, M. J.; Goodson, B. M.; Rosen, M. S.; Chekmenev, E. Y. *J. Magn. Reson.* **2020**, *319*, No. 106813.

https://doi.org/10.1021/acs.analchem.3c05573
Anal. Chem. XXXX, XXX, XXX−XXX